Baroclinic instability of an idealized tidal mixing front

by K. H. Brink[1]

ABSTRACT

Tidal mixing fronts separate vertically homogenized waters from stratified ambient waters. The linear and nonlinear baroclinic stability of an idealized tidal mixing front is treated here in the parameter range that is stable with regard to symmetric instabilities and that has no bottom friction. All model configurations considered are unstable, and the dependence on bottom slope, stratification and other parameters is similar to that suggested by models (such as that of Blumsack and Gierasch, 1972) with much simpler configurations. The finite-amplitude evolution of the instabilities is treated using a primitive equation numerical model. The initial length scale and growth rate of the instabilities are well predicted by the linear calculations. As the system evolves, gravitational potential energy is transferred to eddy kinetic energy, which peaks at about the time that potential energy stops decreasing. The peak eddy kinetic energy depends strongly on the bottom slope, with the greatest values occurring when the bottom and near-bottom isopycnals slope in the same direction. As the fields continue to evolve, eddy kinetic energy decreases, mean kinetic energy increases, and the eddies become larger and more barotropic. The horizontal eddy mixing coefficient is estimated at the time of maximum lateral heat flux and is found to be sensitive to the magnitude of the bottom slope but not its sign. Overall, the instability and the related eddy mixing are strong enough to encourage the idea that these instabilities might be effective at a more realistic tidal mixing front.

1. Introduction

Among the most biologically productive regions in the global coastal ocean are those vertically homogenized by tidally induced turbulence, which are typically bounded by a tidal mixing front. This front (e.g., Fig. 1) separates shallower, well-mixed waters from deeper, stratified waters, and it occurs where the stabilizing surface heat fluxes exactly balance the tendency of tidally driven bottom boundary layer turbulence to homogenize the water column. The front's location thus obeys the famous h/q^3 criterion (where h is the water depth and q is a representative tidal current amplitude) (Simpson and Hunter, 1974), which requires that tidal mixing fronts generally parallel topography and thus usually intersect a sloping bottom.

One substantial question arises about the productivity of these tidally mixed areas. Specifically, if biological activity in the mixed waters is sustained over time, one would expect a

1. Department of Physical Oceanography, Woods Hole Oceanographic Institution, Woods Hole, Massachusetts, 02543, U.S.A. *email: kbrink@whoi.edu*
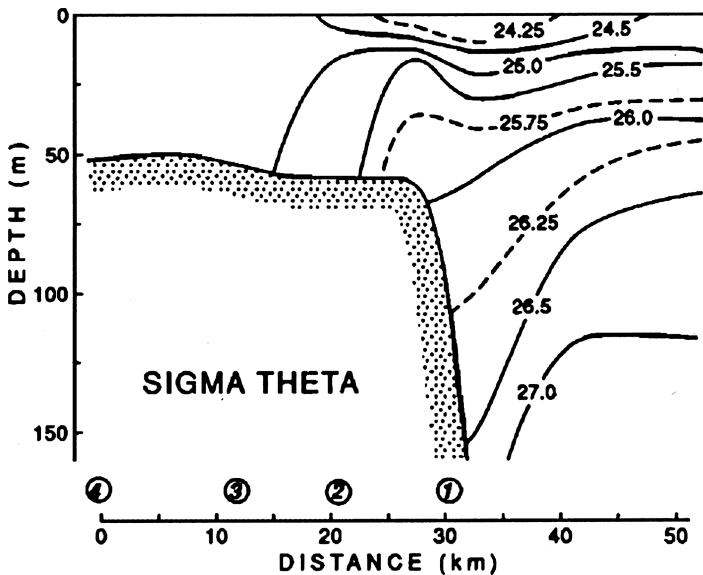
Figure 1. A typical density (σ_t) section across the northern side of Georges Bank, July 3, 1988. From Loder *et al.* (1992). An edited version of this paper was published by the American Geophysical Union. Copyright 1992 American Geophysical Union.

flux of nutrients from the stratified ambient waters into the mixed region. This follows from the idea that the productivity cannot rely completely on recycled nutrients. Franks and Chen (1996) provide a very reasonable replication of this flux in a two-dimensional numerical model of tides and the mixing front.

The two-dimensional model, however, does not embrace the only potential means to transport nutrients through a tidal mixing front. Garrett and Loder (1981), for example, suggest a range of possibilities that include wind driving and eddy transports associated with frontal instabilities. Since then, steady circulations have been investigated more deeply by Loder and Wright (1985), and wind driving by Chen *et al.* (2003). There is plentiful evidence for tidal mixing front instability around the British Isles (e.g., Simpson and James, 1986), although this possibility is rarely mentioned in the context of Georges Bank, a tidally mixed area off the eastern coast of North America. There have been a number of studies of the stability of tidal mixing fronts, but these have been very idealized or realistically complex. In the idealized category, van Heijst (1986) treats an inviscid case with a flat bottom and two immiscible layers. Some laboratory experiments (van Heijst, 1986; Thomas and Linden, 1996) also treat similarly idealized situations. Among numerical models, James (1989) treats a simple case but without tides, while Badin *et al.* (2009) find evidence for frontal instability in their very complete simulation runs.

As an instability problem, the tidal mixing front has a couple of interesting, relatively unique features. One is that the origin of the front depends on waters being vertically

homogenized by turbulence generated at the bottom. Thus, in a realistic context, bottom stress is of lowest order importance in defining the basic state and, presumably, for a growing instability as well. Second, the front itself is expected to move back and forth across isobaths with the tides. This sort of oscillation in the background flow has been shown, for a simpler context, to enhance the growth of instabilities under at least some conditions (Poulin *et al.*, 2003; Flierl and Pedlosky, 2007).

Their purpose of this contribution is to provide a first step in a systematic study of instability and associated cross-frontal exchange at a tidal mixing front. The starting point is to consider steady fronts that have the structure of an idealized tidal mixing front but that are not affected by bottom friction. Further, attention here is also confined to the case where the front is stable with regard to symmetric instabilities (e.g., Stone, 1966). Given these constraints, the linear instability and finite-amplitude evolution of the front still require an investigation of a parameter space that includes the influences of bottom slope, stratification, frontal width and rotation. Future contributions will deal first with slantwise convection and bottom friction, and later with a realistic, oscillating, tidal mixing front. In the end, while frontal instability is central to the issues at hand, the real goal is to quantify the extent to which the resulting eddy field can effect exchanges across the front.

One important point of comparison in the following calculations is the quasigeostrophic linear stability model of Blumsack and Gierasch (1972: BG72 henceforth), who considered a case with spatially uniform stratification and constant vertical shear over a uniformly sloping bottom. When the bottom is flat, the maximum growth rate occurs at a scale similar to the internal Rossby radius of deformation, and the instability has no long-wave cutoff. When the bottom slopes in the opposite direction from the isopycnal slope (positive slope, in the notation of the following sections), the maximum instability occurs at shorter scales, while the maximum growth rate decreases, but never vanishes, with increasing slope. When the bottom slopes in the opposite sense (i.e., in the same direction as isopycnals), the maximum growth rate and the most unstable wavelength both increase until they reach a maximum. Beyond this point, both the growth rate and wavelength decrease until the instability vanishes when the bottom slope exceeds the isopycnal slope. There is always a short wavelength cutoff for instability, and there is a long-wave cutoff, as well, when the bottom slope is nonzero. Overall, a bottom slope in the same direction as the isopycnal tilt increases instability (up to a point), and the opposite slope decreases the instability. At first glance, this might seem to contradict Barth's (1989) findings for an upwelling front, but in his case, the tilting isopycnals intersect a level upper surface, and not the sloping bottom. Despite the very simple (as compared with a tidal mixing front) configuration of BG72, their results provide useful context in the following.

2. Formulation

a. The physical configuration

In all cases treated here, the basic state (Fig. 2) consists of mean flow along the axis of a channel of width W. One side of the channel (larger x) has uniform density stratification, and
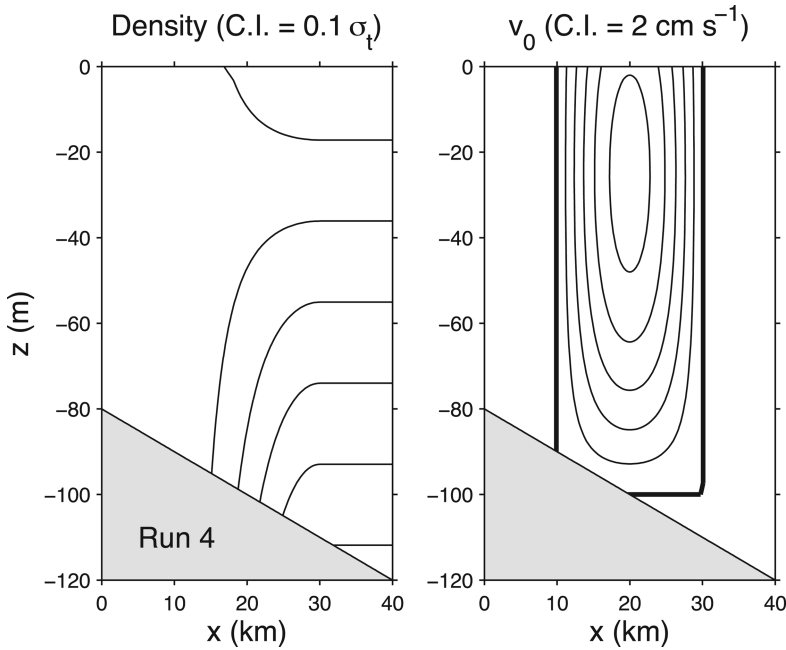
Figure 2. Representative initial conditions for either a linear or nonlinear stability calculation, here for case 4 (Table 1). The left panel is initial density (contour interval: 0.1 σ_t unit). The right panel is initial along-channel velocity. Positive and zero contours are heavy, and negative contours are lighter lines (contour interval: 2 cm s^{-1}).

buoyancy frequency N_0. The opposite side of the channel has very weak initial stratification, if any. Between these two regions, there is a mean along-channel flow $\bar{v}$ in thermal wind balance with the mean density field $\bar{\rho}$. The level of no motion is at the mean depth of the channel, H. Specifically, the fields are given by

$$\bar{\rho}(x, z) = \rho_0 \qquad \text{for } x < W/2 - L, \tag{1a}$$

$$\bar{\rho}(x, z) = \rho_0 \left\{ 1 - \left[1 + \sin \left(\frac{\pi(x - W/2)}{2L} \right) \right] N_0^2 (z - z_0)/(2g) \right\}$$

$$\text{for } W/2 - L < x < W/2 + L, \text{ and} \tag{1b}$$

$$\bar{\rho}(x, z) = \rho_0 [1 - N_0^2 (z - z_0)/g] \qquad \text{for } x > W/2 + L, \tag{1c}$$

so that

$$\bar{v}(x, z) = 0 \qquad \text{for } |x - W/2| > L, \text{ and} \tag{2a}$$

$$\bar{v}(x, z) = \frac{\pi}{8fL} \cos \left[\frac{\pi(x - W/2)}{2L} \right] N_0^2 (z + H)[(z - H) - 2z_0]$$

$$\text{for } |x - W/2| < L. \tag{2b}$$

The Coriolis parameter is f, the acceleration due to gravity is g, ρ_0 is the background density of the water, $-z_0$ is the depth of the velocity maximum and L is the half width of the frontal region. Attention here is restricted to the range where the maximum velocity occurs at or above mid-depth: i.e., where $-H/2 \leq z_0 \leq 0$, so that the mean along-channel flow is in the same direction for $-H \leq z$.

The water depth h varies in the cross-channel direction:

$$h = H + \alpha(x - W/2), \tag{3}$$

so that the depth at mid-channel, i.e., at the center of the front, is the average channel depth.

The vorticity associated with the flow field is

$$Q = -\rho_z(v_x - u_y + f) + \rho_x v_z - \rho_y u_z \tag{4}$$

where subscripts with regard to an independent variable represent partial differentiation. The cross-channel, along-channel and vertical velocity components are (u, v, w), respectively, and (x, y, z) are the corresponding coordinates. Attention here is restricted to cases where the initial vorticity is positive everywhere, i.e., where symmetric instabilities and slantwise convection are not possible (e.g., Stone, 1966).

b. Linear stability formulation

The linear stability problem is addressed by linearizing about conditions (1) and (2), so that for the present purposes, (u, v, w, p, ρ) represent perturbations, while the same quantities with overbars represent the mean state. The governing equations for the perturbations are then

$$v_t + u\bar{v}_x + \bar{v}v_y + w\bar{v}_z + fu = -\rho_0^{-1} p_y, \tag{5a}$$

$$u_t + \bar{v}u_y - fv = \rho_0^{-1} p_x, \tag{5b}$$

$$0 = -p_z - g\rho, \tag{5c}$$

$$u_x + v_y + w_z = 0 \text{ and} \tag{5d}$$

$$\rho_t + u\bar{\rho}_x + \bar{v}\rho_y + w\bar{\rho}_z = 0 \tag{5e}$$

In order to maintain static stability, a relatively weak background stratification (N^2 of 0.5% of the maximum value) is added everywhere. This keeps the numerical solutions to the vorticity equation resulting from (5) well behaved in the otherwise unstratified region. The system (5) is reduced to a single equation for perturbation pressure p, and solved subject to a rigid lid at the surface:

$$w = 0 \quad \text{at } z = 0, \tag{6a}$$

no flow through the channel walls:

$$u = 0 \quad \text{at } x = 0, W, \tag{6b}$$

and no flow normal to the bottom:

$$w + h_x u = 0 \quad \text{at } z = -h. \tag{6c}$$

The solution is assumed to have the form

$$p = \hat{p}(x, z) \exp[i(\omega t + ly)], \tag{7}$$

where the along-channel wavenumber is l and the frequency ω is complex. The problem for $\hat{p}$ is then solved numerically for a given l via resonance iteration for the complex frequency on a vertically stretched grid (Brink, 2006), with 120 grid points in x and 40 in z. This approach requires making an initial guess at the complex frequency, and it requires searching to make sure the fastest growing modes are actually obtained. The nominal accuracy for the resulting frequency estimates is 0.1%. Given the results of these calculations, it is straightforward to compute the energy transfers, notably that of mean potential energy per unit mass to eddy potential energy per unit mass:

$$C_{MPE \rightarrow EPE} = \frac{g}{\rho_0} \int_0^W \int_{-h}^0 < u\rho > \frac{\overline{\rho_x}}{\overline{\rho_z}} dz dx, \tag{8a}$$

(where $<>$ denotes an along-channel and time mean over a wavelength and period, respectively), which is the signature of baroclinic instability. For comparison, the conversion from mean kinetic energy to eddy kinetic energy per unit mass is

$$C_{MKE \rightarrow EKE} = - \int_0^W \int_{-h}^0 \left[< uv > \overline{v_x} + < wv > \overline{v_z} \right] dz dx \tag{8b}$$

c. Nonlinear stability

The nonlinear stability calculations take advantage of the Regional Ocean Modeling System (ROMS) (e.g., Shchepetkin and McWilliams, 2005). In dealing with the nonlinear problem, variables such as u and v no longer represent perturbations and are governed by

$$u_t + uu_x + vu_y + wu_z - fv = -\rho_0^{-1} p_x + (Du_z)_z \tag{9a}$$

$$v_t + uv_x + vv_y + wv_z + fu = -\rho_0^{-1} p_y + (Dv_z)_z, \tag{9b}$$

$$0 = -p_z - g\rho, \tag{9c}$$

$$u_x + v_y + w_z = 0, \tag{9d}$$

$$\rho_t + u\rho_x + v\rho_y + w\rho_z = (B\rho_z)_z, \text{ and} \tag{9e}$$

$$\rho = \rho_0[1 - \gamma(T - T_0)], \tag{9f}$$

where T_0 is a reference temperature (14 °C), the thermal expansion coefficient for water is $\gamma(= 1.7 \times 10^{-4} \text{ °C}^{-1})$, and the vertical turbulent viscosity and mixing coefficients D and

B, respectively, are found using the Mellor-Yamada level 2.5 turbulence closure scheme (e.g., Wijesekera *et al.*, 2003). There is no explicit lateral mixing or viscosity in any model run. The system is solved with a free surface boundary condition, free slip at vertical walls, and no flow through the bottom. No turbulent heat fluxes are allowed through any boundary. At the bottom, no stress is allowed, so

$$u_z = v_z = 0, \tag{10}$$

consistent with the drag coefficient c_D vanishing. For the parameter range used here (where the horizontal scales are small compared to the barotropic Rossby radius of deformation), there is little difference between using a rigid lid or free surface condition.

Numerical experiments are initialized with conditions (1) and (2), and a zero-mean white random noise (amplitude of 0.0001 m) is added to the initial free surface height to help stimulate the eventual instability. The problem is solved in a cyclic channel of length 100 km ($\Delta y = 0.25$ km) and width $W = 40$ km ($\Delta x = 0.4$ km). Thirty terrain-following vertical levels are used, with a concentration of grid points near the lower boundary (this concentration was done for consistency with runs, to be reported elsewhere, that include bottom friction). The model runs include a passive tracer, initialized to 1 for $x > W/2$ and 0 for $x < W/2$. The model takes advantage of the default 4th order centered advection scheme for momentum, and a recursive method ("TS_MPDATA") scheme for temperature and tracer advection. All model runs proceed for 100 days, which is sufficient to allow the flow field to reach a fully developed finite-amplitude state. A few model runs, with Rossby number $|v_x|/f > 1$, evolve primarily through a slumping motion that is uniform in y. These runs are excluded from consideration: all reported model runs develop eddies typically having initial along-channel wavelengths less than about 20 km.

Some useful diagnostic quantities for the primitive equation runs include the total kinetic energy, mean kinetic energy, the eddy kinetic energy and the potential energy, all per unit mass:

$$TKE = \frac{1}{2} \int_0^W \int_{-h}^0 [u^2 + v^2] dz dx, \tag{11a}$$

$$MKE = \frac{1}{2} \int_0^W \int_{-h}^0 [\{u\}^2 + \{v\}^2] dz dx, \tag{11b}$$

$$EKE = \frac{1}{2} \int_0^W \int_{-h}^0 [u'^2 + v'^2] dz dx, \tag{11c}$$

$$PE = \frac{1}{\rho_0} \int_0^W \int_{-h}^0 [g\rho z - g\rho_0 \xi_0] dz dx, \tag{11d}$$

where { } indicates an along-channel mean, ( )′ is a deviation from that mean and ξ_0 is an arbitrary reference height. Note that the form of (11d) does not lend itself to distinguishing between mean and eddy potential energy. The key energy conversions used below are between potential energy and kinetic energy:

$$C_{PE \to KE} = -\frac{g}{\rho_0} \int_0^W \int_{-h}^0 \{w\rho\}dzdx,$$ (12a)

and between mean kinetic energy and eddy kinetic energy per unit mass:

$$C_{MKE \to EKE} = -\int_0^W \int_{-h}^0 [\{v_x\}\{u'v'\} + \{v_z\}\{w'v'\} + \{u_x\}\{u'u'\} + \{u_z\}\{w'u'\}]dzdx.$$ (12b)

The mean-to-eddy conversion terms that involve $\{u\}$ are in practice very small relative to the $\{v\}$ terms in all that follows.

d. Parameters

The systems (5) or (9) can be nondimensionalized, scaling z by H, (x, y) by $\Lambda = N_0 H/f$, t by f^{-1}, (u, v) by V and density changes by $\rho_0 N_0 V/g$. The scale strength of the along-channel flow is estimated using the geometry of Figure 2 and the thermal wind equation as

$$V \approx -\frac{(H + z_0)^2 N_0^2}{2fL}.$$ (13a)

The scalings lead to a Froude number

$$F = \frac{|V|}{N_0 H},$$ (13b)

or (using 13a)

$$F \approx \frac{(H + z_0)^2 N_0}{2fLH}.$$ (13c)

F is equivalent to a Rossby number for this scaling. In addition, (13a) or the initial conditions, (1) and (2), lead to the parameter

$$\eta = (H + z_0)/H,$$ (13d)

and the bottom boundary condition (6c) leads to a slope Burger number

$$s = \alpha N_0/f,$$ (13e)

so that the nondimensional bottom boundary condition becomes

$$w + su = 0. \tag{13f}$$

Notice that, because α can change sign, s can be either positive or negative. The positive sense (deeper water is stratified, as shown in Fig. 2) is what one would normally expect for a tidal mixing front.

3. Linear stability

The linear stability problem, (5)–(7), is treated for 32 examples (Table 1), representing cases with differing α, N_0, f, L, z_0 and H. The actual choice of parameters is somewhat constrained by the avoidance of cases (including all cases having roughly $s < -0.2$) that are gravitationally unstable or are unstable to slantwise convection, i.e., that have $\bar{Q} < 0$. All cases in Table 1 are unstable, and when α ≤ 0, there is no long-wave cutoff for ω_l, the imaginary part of the frequency (e.g., Fig. 3a). When α > 0 (the sense of a normal tidal mixing front), there is usually, to within the program's numerical accuracy, a long-wave cutoff (e.g., Fig. 3b), but there is no obvious pattern in terms of the nondimensional numbers for when this occurs. No examples of a short-wave cutoff are found, at least partly because the numerical results lose accuracy and are terminated for larger wavenumbers. However, based, for example, on Roullet *et al.* (2012), one might expect that there is no short-wave cutoff here because the density fronts intersect the boundaries. Results in Table 1 are summarized as the maximum eddy kinetic energy growth rate A (the maximum with regard to l of $-2\omega_l$), and the wavelength of maximum instability λ. In all cases, the instability is clearly baroclinic: the conversion $C_{MPE-EPE}$ (8a) is orders of magnitude larger than that associated with transfer from mean kinetic energy to eddy kinetic energy (8b).

The spatial structures of the most unstable modes are examined for the cross-channel velocity component. With the mean velocity maximum at mid-depth ($z_0 = -H/2$) and with α = 0, the structure is symmetric about mid-depth (Fig. 4, left panel). For the cases with maximum mean velocity shallower than mid-depth ($z_0 > -H/2$), there are distinct surface- and bottom-trapped modes, where a bottom-trapped mode is always the most unstable if α = 0 (e.g., Fig. 4, middle panel). With a sloping bottom, there are again always surface- and bottom-trapped modes, and the bottom-trapped mode is often (but not always) the most unstable (e.g., Fig. 4, right panel).

Inspection of the model outputs shows that the maximum growth rate increases as the mean velocity maximum approaches the surface (i.e., as $z_0 \to 0$; e.g., compare runs 1 and 2), which also increases the magnitude of the mean velocity for a given f, L and N_0. Because (13c) shows that a shallower maximum corresponds to a larger Froude number, this increased instability is not surprising. Further, the wavelength of maximum instability λ also increases as the mean flow maximum approaches the surface (i.e., as $-z_0$ decreases). There is clearly a strong dependence on the bottom slope (e.g., compare runs 2, 4, 9, 12,

Table 1. Summary of linear model runs.

Run	$f \times 10^4$ (s^{-1})	$-z_0$ (m)	H (m)	α	$N^2 \times 10^4$ (s^{-2})	L (km)	s	F	η	A (day^{-1})	λ (km)
1*	1	50	100	0	1	10	0	0.125	0.5	1.66	9.8
2*	1	25	100	0	0.5	10	0	0.20	0.75	1.67	10.5
3*	0.5	50	100	0	0.5	10	0	0.18	0.5	0.96	13.7
4*	1	25	100	0.001	0.5	10	0.07	0.20	0.75	1.44	8.8
5	1	50	100	0.001	1	10	0.1	0.125	0.5	1.57	9.2
6	1	50	100	−0.001	1	10	0.1	0.125	0.5	1.52	8.5
7*	1	0	100	0.001	0.5	10	0.07	0.354	1.0	2.05	13.1
8	1	50	100	0.0005	0.5	10	0.04	0.088	0.5	1.14	6.8
9*	1	25	100	0.0005	0.5	10	0.04	0.199	0.75	1.57	9.2
10	1	50	100	0.0015	0.5	10	0.11	0.088	0.5	1.11	6.6
11	1	50	100	0.0015	1	10	0.15	0.125	0.5	1.56	9.4
12*	1	25	100	0.0015	0.5	10	0.11	0.199	0.75	1.32	8.3
13*	1	25	100	0.0015	1	10	0.15	0.281	0.75	1.82	12.3
14	1	50	100	0.001	0.5	10	0.07	0.088	0.5	1.33	8.5
15*	1	25	100	0.001	0.5	10	0.07	0.199	0.75	1.94	11.2
16*	1	0	50	0	0.5	10	0	0.177	1.0	1.20	7.06
17*	1	25	100	0.0025	1	10	0.25	0.281	0.75	1.45	11.6
18*	1	25	100	0.0025	0.5	10	0.18	0.199	0.75	1.08	6.9
19*	1	50	100	0.0025	1	10	0.25	0.125	0.5	1.08	6.9
20*	1	0	100	0.0025	0.5	10	0.18	0.354	1.0	1.68	11.4
21*	1	25	100	0.0025	0.5	10	0.18	0.199	0.75	2.26	14.0
22*	1	50	100	0	0.5	20	0	0.044	0.5	0.62	7.1
23*	1	25	100	0	0.25	10	0	0.14	0.75	1.19	7.4
24*	1	25	100	0	0.117	10	0	0.096	0.75	0.83	5.1
25	1	25	100	0.0015	0.5	10	0.11	0.199	0.75	2.04	12.3
26*	1	25	100	0.004	0.5	10	0.28	0.199	0.75	2.64	14.6
27*	1	25	100	0.004	0.5	10	0.28	0.199	0.75	0.76	5.5
28*	1	50	150	0.0065	0.5	10	0.46	0.236	0.67	0.99	7.0
29	1	50	150	0.0065	0.5	15	0.46	0.157	0.67	0.66	7.5
30*	1	75	200	0.0090	0.5	10	0.63	0.276	0.63	1.56	10.3
31*	1	25	100	0.0018	0.5	10	0.13	0.199	0.75	2.11	12.8
32*	1	0	100	0.004	0.25	10	0.20	0.25	1.0	2.26	6.7
										2.31	14.0

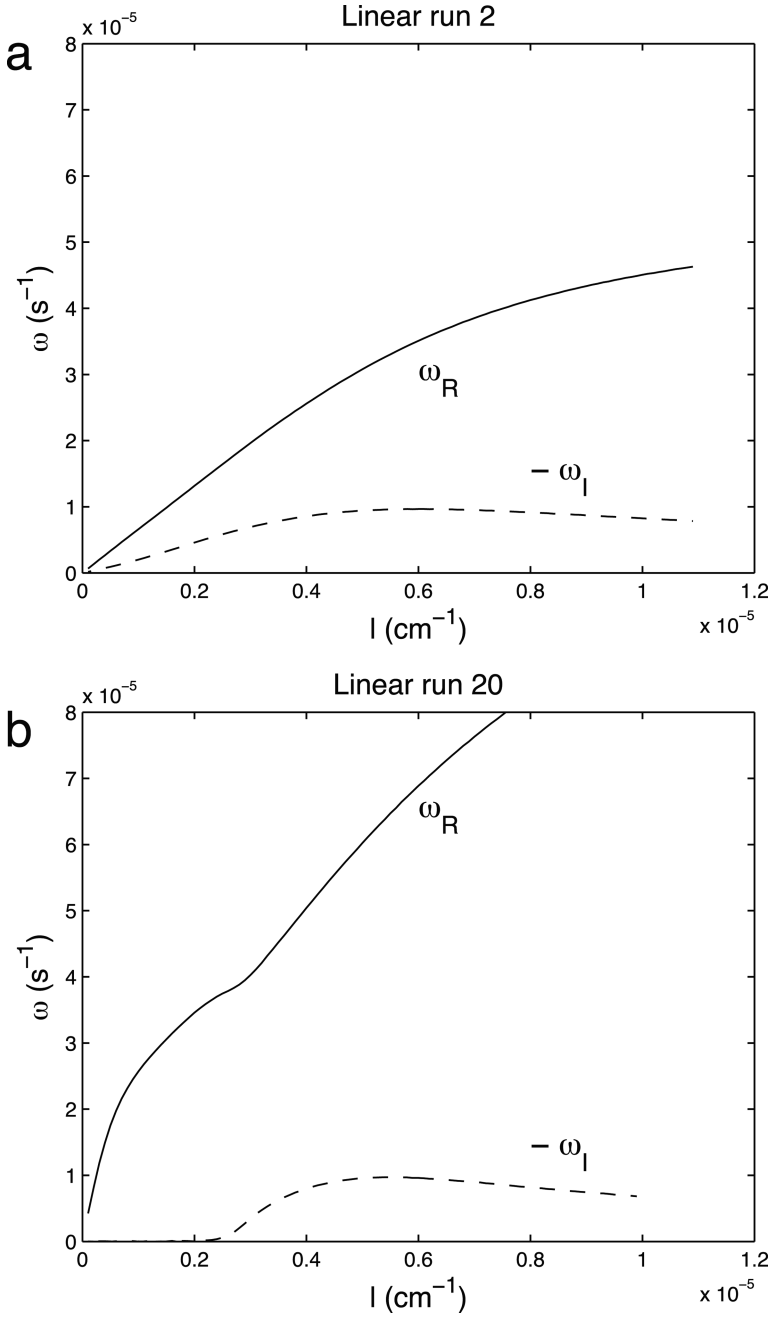*Case for which a nonlinear numerical model run was also conducted.

Figure 3. Representative dispersion curves for the most unstable waves in two linear cases. Run 2 (a, upper panel) has no long-wave cutoff, while run 20 (b, lower panel) has a long-wave cutoff. In each panel, the real part of the frequency is shown as a solid line, while the imaginary part is shown as a dashed line.
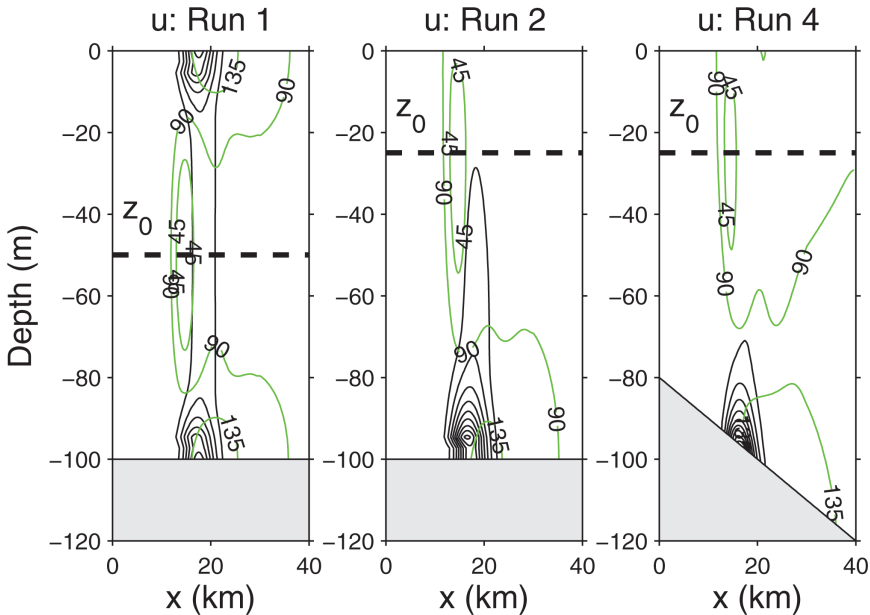
Figure 4. Cross-channel velocity u modal structure for the most unstable wave modes in three cases. The lighter contours are modal amplitude (arbitrary units) and the green contours show the phase.

15, 18, 21, 25, 27 and 31). When the bottom slope is in the same direction as the near-bottom isopycnal slope ($\alpha < 0$), the growth rate of the instability is relatively large (as is its wavelength), but when the bottom slope is counter to the isopycnal slope ($\alpha > 0$), the maximum growth rate and wavelength decreases as the slope increases. This sense of bottom effect is the same as that found, with a simpler flow geometry, by BG72.

Values for the most unstable growth rates and wavelengths collapse very conveniently onto single curves described by nondimensional parameters. Specifically, the fit (using all runs in Table 1, except for run 32, where two nearly equal peaks, for different l values, are found for the growth rate)

$$A = \frac{a_1 f(F/\eta)}{1 + b_1 s} \tag{14a}$$

yields a correlation of 0.95 and $a_1 = 0.71$, $b_1 = 1.5$ (Fig. 5a). For the most unstable wavelength,

$$\lambda = \frac{a_2 \Lambda \eta}{1 + b_2 s} \tag{14b}$$

yields a correlation of 0.96 and $a_2 = 1.9$, $b_2 = 1.3$, with the same set of 31 runs (Fig. 5b). Given the range of parameters in the calculations (Table 1), these expressions should not

a

$$(A/f) = a_1(F/\eta)\,/(1 + b_1 s)$$
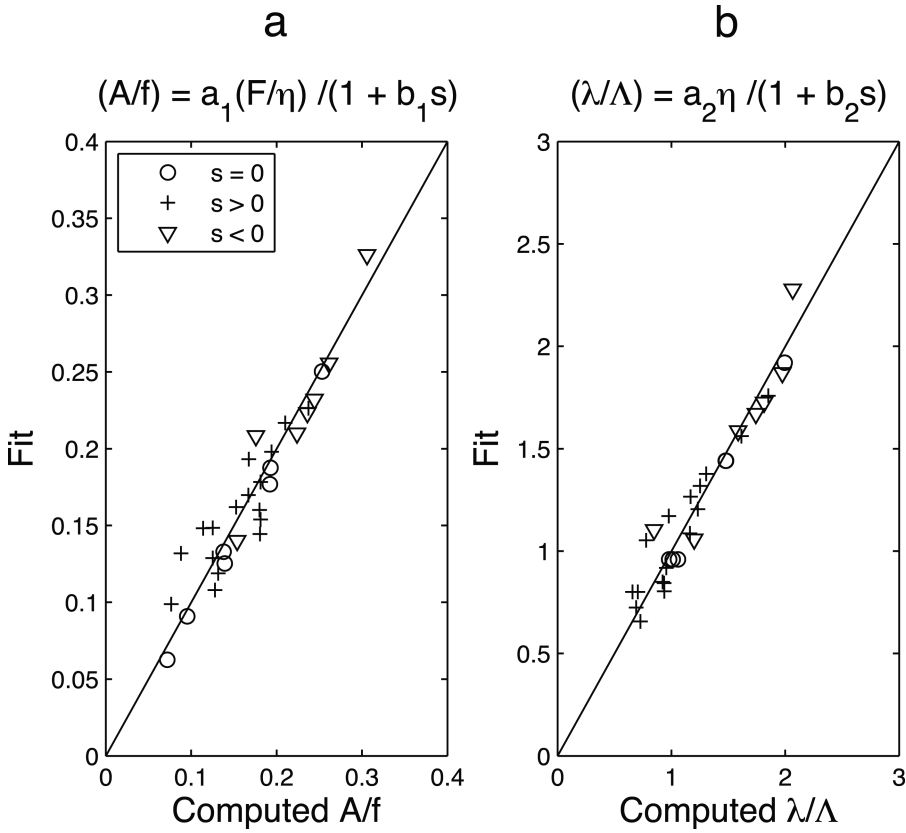
b

$$(\lambda/\Lambda) = a_2\eta\,/(1 + b_2 s)$$

Figure 5. Comparison of the fits (14) to results of the linear stability analysis. Left panel (a): normalized maximum growth rate. Right panel (b): wavelength of the most unstable wave.

be taken as reliable for $s < -0.2$, and so there is no reason to suppose that either A or λ actually reach infinite values. An alternative parameterization (motivated by BG72, or Isachsen, 2011) replaces s in (14) by the ratio of the bottom slope to the isopycnal slope ($s\eta/F$ in the present notation). This modified functional form performs only very slightly worse than does (14), e.g., a correlation of 0.93 vs. 0.95 in the fit for A.

The form of (14b) suggests that the appropriate internal Rossby radius for scaling is that based on the distance from the bottom to the velocity maximum, $(H + z_0)$, rather than on the mean total depth H. Likewise, it is interesting to note that, as $b_2 s$ becomes large, the instability scale obeys

$$\lambda \to \frac{a_2(H + z_0)}{b_2\alpha} \qquad \text{for } s\,b_2 \gg 1, \tag{15}$$

i.e., the limiting wavelength (or rate) of maximum instability does not depend on the stratification.

4. Nonlinear stability and evolution

A sequence of 24 primitive equation numerical model runs (Table 1, runs denoted by asterisks) is executed with initial conditions in the form (1) and (2). In order to maximize intercomparison, all of these runs duplicate one of the linear stability cases. The initial instability is characterized by the growth rate A of eddy kinetic energy per unit mass (EKE), where "eddy" is taken to mean the deviation from the along-channel mean at an (x, z) location. The growth rate is estimated by fitting the EKE integrated over $x = 10$–30 km to an exponential over a moving 3-day time window, and then picking the peak value occurring just before the instability reaches finite-amplitude (e.g., before a typical eddy velocity exceeds about 0.005 m s^{-1}). The dominant along-channel wavelength is found by computing an average (weighted by energy) along-channel autocovariance function for mid-depth and shallow cross-channel velocity u. The dominant wavelength is taken as four times the lag to the first zero crossing at the time when the growth rate A is estimated. At early stages of the instability (Fig. 6, left panel), the perturbation is relatively monochromatic and sinusoidal alongshore. The initial growth rates and wavelengths compare rather well against the results of the linear stability analysis (Fig. 7: correlations of 0.99 and 0.95 for A and λ, respectively). A further comparison against linear theory can also be made by comparing snapshots of the small-amplitude cross-channel velocity (Fig. 8) with the corresponding linear stability modal structures (Fig. 4). This comparison, of course, is only qualitative because a single snapshot cannot account for the phase variations of the linear result. Nonetheless, the nonlinear results do agree in terms of the general amplitude distribution.

The longer-term evolution follows a similar pattern for all runs. The initial stages of the instability (days 19–40 in Fig. 9a and 20–30 in Fig. 9b) are typified by a transfer of energy from potential to eddy kinetic energy (Equation 12a), where "eddy" is defined as deviations from an along-channel mean. For all model runs, the potential energy (11d) (integrated over the entire channel) decreases during the time of eddy kinetic energy (11c) growth, and then remains relatively constant. In most cases, the mean kinetic energy (11b) also decreases during this growth phase. Eddy kinetic energy usually peaks at the end of this monotonic transfer period, and its peak value is reasonably well correlated (0.81) with the square of the linear growth rate. As eddy kinetic energy increases to finite amplitude, the exchanges between eddy and mean kinetic energy grow and eventually dominate the energy transfers. However, the sense of this eddy-to-mean transfer (12b) typically alternates wildly, but the net exchange (after peak eddy kinetic energy) is generally from eddy to mean kinetic energy. Of the 24 finite-amplitude runs, all but four show a net increase (relative to the initial state) of mean kinetic energy by the end of the 100-day run. Of the four that do not show an increase, most have an upward mean kinetic energy trend near the end of the run and do

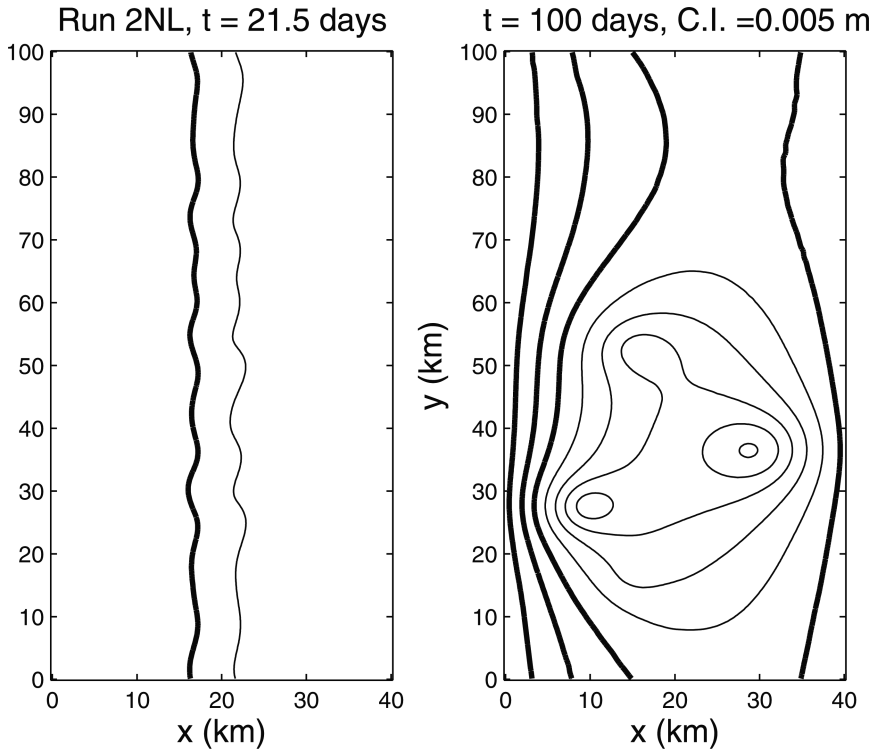## Run 2NL, t = 21.5 days   t = 100 days, C.I. =0.005 m

Figure 6. Plan view of sea surface elevation ζ for finite amplitude run 2. Zero and positive contours are shown as heavy lines, while negative contours are lighter lines. The contour interval is 0.005 m. Left panel, day 21.5, in the early stages of instability growth. Right panel, day 100, after most of the vortices have consolidated.

not appear to have reached a statistically steady state. In all cases, the total energy (sum of potential, eddy kinetic and mean kinetic) decreases over the course of a model run, by an amount small compared to, say, the change in potential energy. The energy loss is primarily due to dissipation associated with vertical shears in the interior of the water column, since there are no stresses at any of the boundaries.

The final mean states (Figs. 6 and 10) are radically different from the initial states. The initial states are always typified by a confined jet at mid-channel, and by temperature fronts that intersect the bottom, and often surface, boundary. On the other hand, the final along-channel mean states (averaged over the last 10 model days: Fig. 10a–c, right panels) typically have mean along-channel flows that are relatively barotropic and that are approaching a monotonic cross-channel shear, i.e., approaching a state where $\{v_x\} > 0$ everywhere. (The example in Fig. 10b has not yet reached such a statistically steady state, and it is also one of the few runs, seemingly unequilibrated, where the final mean kinetic energy is not greater

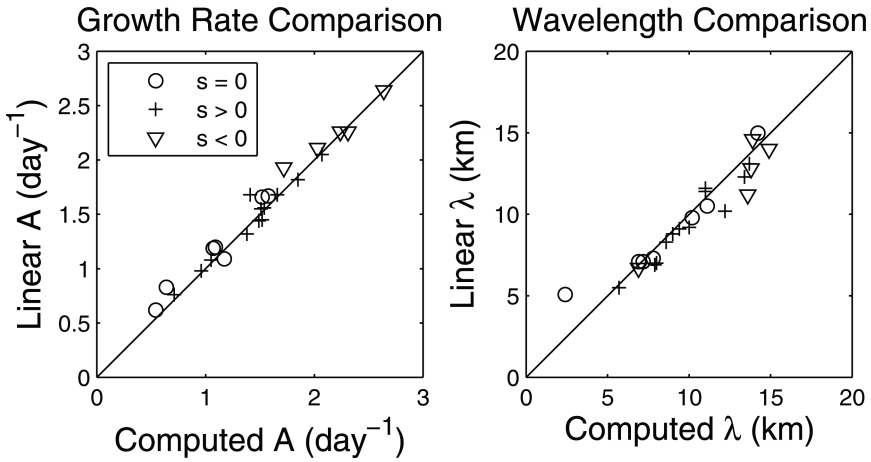## Growth Rate Comparison

Wavelength Comparison

Figure 7. A comparison of the initial growth rates (left panel) and most unstable wavelength (right panel) for the linear stability calculations and for the early phase of finite-amplitude stability.
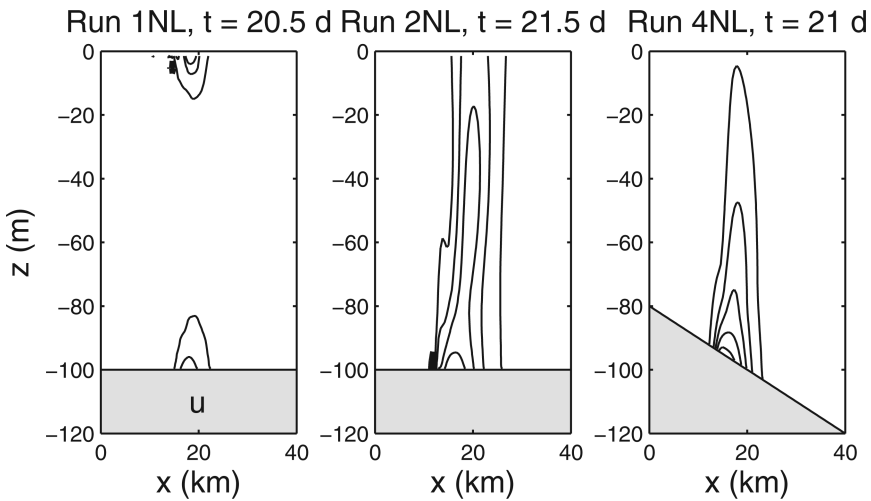
Figure 8. Instantaneous cross-channel velocity *u* fields for three finite-amplitude runs that correspond to the linear examples in Figure 4. Times are chosen to be early in the growth of the finite-amplitude instability.

than its initial value.) Further, the final temperature field always approaches a state where the nearby isotherms parallel the surface and bottom boundaries. The same statements could be made of individual cross-channel sections sampled at along-channel locations away from active eddies. In the quasigeostrophic limit, a field with monotonic lateral velocity shear and isotherms parallel to solid surfaces would be expected to be baroclinically stable, e.g.,
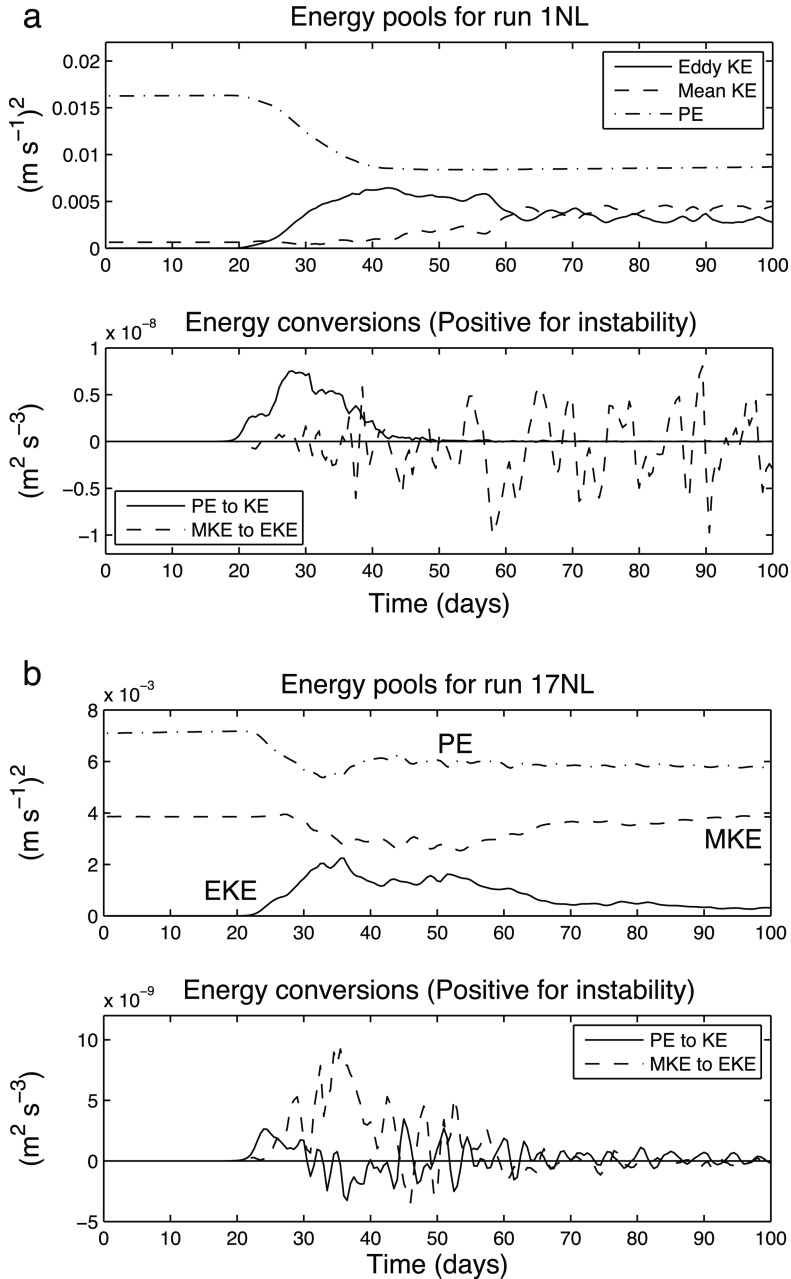
Figure 9. Evolution of finite-amplitude runs 1 (a, upper pair) and 17 (b, lower pair). The upper panel in each pair shows potential energy (PE), eddy kinetic energy (EKE) and mean kinetic energy (MKE), all per unit mass. The lower panel in each pair shows conversion from potential to kinetic energy (solid line) and from mean kinetic energy to eddy kinetic energy (dashed line).
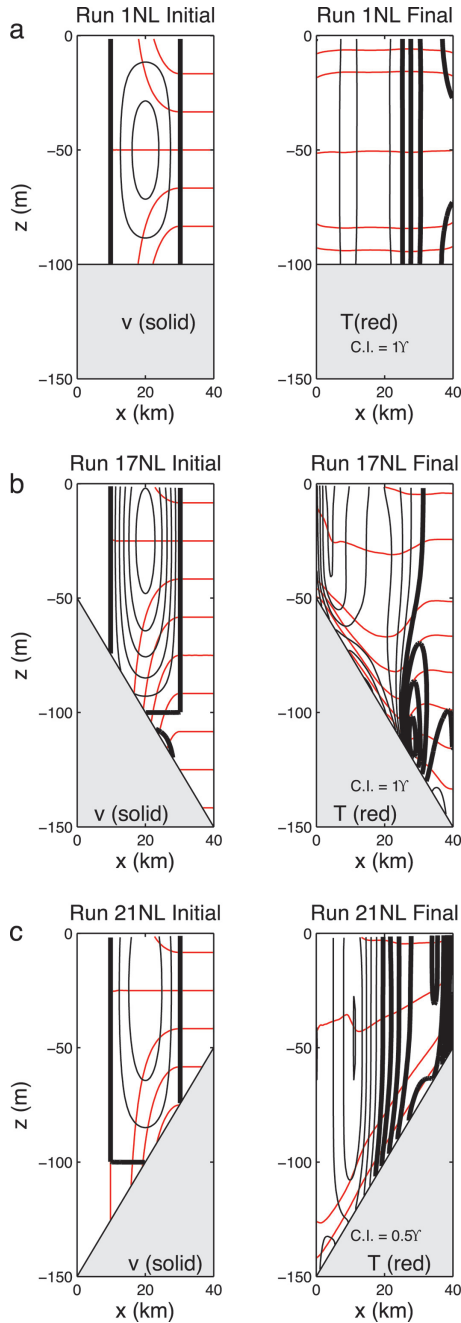
Figure 10. Initial (left) and final (right) mean along-channel velocity v and temperature T for finite-amplitude runs 1 (a, upper pair), 17 (b, middle pair) and 21 (c, lower pair). Red contours are temperature (1 °C contour interval in a and b, but 0.5 °C in c), heavy black contours are zero or positive along-channel velocity (contour interval = 0.04 m sec^{-1} for all panels), and light-black contours are for negative along-channel velocity. The means in the right-hand panels are over the last 10 days and over the entire channel length.
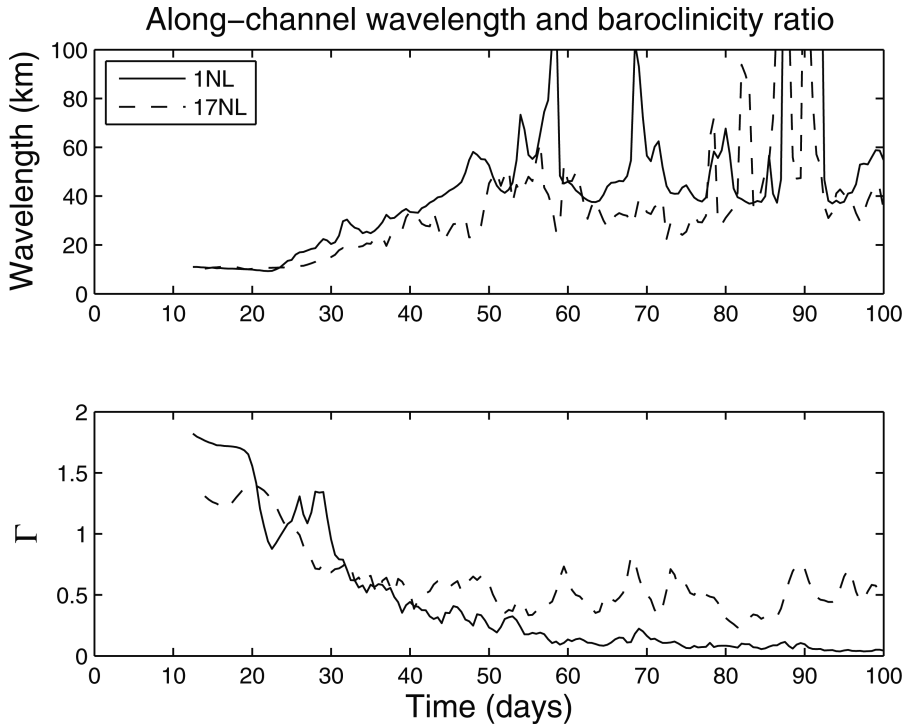
Figure 11. Time evolution of along-channel wavelength (upper panel) and baroclinicity ratio (16) for finite-amplitude runs 1 (solid) and 17 (dashed). Small values of Γ correspond to relatively barotropic eddy flow.

Pedlosky (1979, sect. 7.3). This also appears to be true in the present context as well: witness the steadiness of the potential energy pool at larger times (Fig. 9).

The finite-amplitude evolution of the eddy field follows the pattern one might expect from a nonlinear inverse cascade: as time goes by, the eddy field becomes more barotropic and adjusts to larger horizontal scales. This process is diagnosed using two variables. First is the typical along-channel wavelength for u in the upper half of the water column (the calculation, using autocovariance functions, is described above). The second diagnostic is a baroclinity ratio Γ defined as

$$\Gamma(t) = \frac{SD[u(W/2, y, 0, t) - u(W/2, y, -h/2, t)]}{SD\ [[0.5[u(W/2, y, 0, t) + u(W/2, y, -h/2, t)]]]}, \tag{16}$$

where SD represents the standard deviation relative to the along-channel mean. As perspective, a first baroclinic mode has $\Gamma = 2$ with constant stratification, while a perfectly barotropic flow would have $\Gamma = 0$. The evolution of these diagnostics is presented for the same two runs (1 and 17) where energy transfers were diagnosed (Fig. 11). At the early

stages of instability, while eddy amplitudes are relatively small (i.e., for $t < 20$ days for these two runs), the along-channel wavelength is relatively constant at essentially the value expected from linear stability estimates. Likewise, as expected from Figures 4 and 8, the initial instabilities are relatively baroclinic, $\Gamma > 1$ for both cases. As the eddy field reaches finite amplitude ($t > 20$ days), the wavelength increases until about day 50 and then begins to carry out occasional excursions to very large values: this noisiness reflects the poor quality of the statistical estimates when there are only a small number of large eddies present in the channel. At the same time, the eddy field becomes more barotropic, i.e., Γ decreases relatively monotonically. Cases with a sloping bottom, however, never become as strongly barotropic as when the bottom is flat (Fig. 11, lower panel). This failure to reach a strongly barotropic state is perhaps not surprising when one compares the along-channel means (Fig. 10). The flow field is evidently undergoing a traditional nonlinear inverse cascade, as is often found in problems with two-dimensional turbulence (e.g., Rhines, 1977). As the horizontal scale becomes large, it is not surprising that the vertical scale also becomes larger as well: this would follow from simply a scaling of the vorticity equation.

In 15 of the 24 finite-amplitude cases, the model runs are long enough that eddy kinetic energy and along-channel wavelength λ are steady over the last 20 days of the model run. Of these 15 runs, three occur where the bottom is flat. In these three cases, the final λ is in the range of 27–35 km. If the eddies were completely isotropic, and their scale were constrained by the cross-channel width, $W = 40$ km, then one might expect λ of O(40–80 km). For the 12 adjusted runs with nonzero bottom slopes, the final, adjusted wavelength is in the range of 26–100 km. These final wavelengths are uncorrelated (correlation magnitude less than 0.3) with the internal Rossby radius, bottom slope, s, or the linearly unstable wavelength (14b). However, the final wavelength is correlated with the Rhines (1975) scale

$$R = b\sqrt{\frac{U}{\beta}}, \tag{17a}$$

where the typical velocity U is taken to be the square root of *EKE* averaged over the last 20 days, β is the topographic vorticity gradient

$$\beta = \alpha f / H, \tag{17b}$$

and b is an unknown constant. The final wavelength is correlated with R (0.52, significant at 90% confidence), and the constant b is found by regression to be 15 (this value of $b >> 1$ is not so strange if one takes into account the factor of 2π required when comparing a length scale to a wavelength). This relation of R to the final λ is not terribly impressive. Recall that the topographic β (17b) is really only strictly valid in the Rhines scale argument if the flow is barotropic, but the final flow field is not necessarily barotropic: the final value of Γ for the 12 sloping-bottom runs ranges from 0.008 to 0.75. Further, if the Rhines scale is greater than the wavelength imposed by the channel (about 80 km), the length scale will probably never evolve to the Rhines scale. These constraints suggest limiting attention only to equilibrated runs with $\Gamma < 0.3$ and $\lambda < 80$ km, so that the correlation between λ and R

becomes 0.92 for six runs (*b* remains 15). Thus, within the parameter range where it should be expected, the transition from nonlinear eddies to more nearly linear topographic Rossby waves does play a role in limiting the scale evolution.

5. Scalings for the finite-amplitude results

a. Available potential energy

During the course of instability, the eddy kinetic energy that is eventually created ought to be related to the initial available potential energy (APE), even though the extent to which the APE is depleted depends on particular conditions, such as the bottom slope. The APE is defined as the difference between initial potential energy and the potential energy if all of the isopycnal surfaces are adjusted adiabatically to a level state. The gravitational potential energy (neglecting the contribution due to free surface elevation, which is expected to be small, $O[f^2 W^2/(gH)]$, as compared with the contribution due to density variations) of the frontal zone is defined roughly as

$$\Phi = \frac{1}{2LH} \int_{\frac{W}{2}-L}^{\frac{W}{2}+L} \int_{-H}^{0} g\rho z \, dz \, dx. \tag{18}$$

If one were to try to use the actual continuous initial density field (1) to estimate APE, the task would be cumbersome and not very enlightening, since it would have to be done numerically. As a simplification, consider a system consisting of three homogenous layers (Fig. 12). The densities are defined by selecting ρ_1 to be the averaged density between $z = z_0$ and 0 for the stable side of the front. Likewise, ρ_2 is the density at $z = z_0$ on the stable side, and ρ_3 is the density averaged between $z = -H$ and $z = z_0$. The final state is estimated only by considering the frontal zone (i.e., ignoring the initially quiescent region, $|x - W/2| > L$, which could be extended arbitrarily), so that, in the final state, the upper layer depth is $-z_0/2$, for example. For simplicity, the bottom is flat, relying on the assumption that, while a sloping bottom will change the APE, this effect will be less significant than that due to the density structure.

Using these starting assumptions, the APE scale is found to be

$$E_0 = \frac{\rho_0 N_0^2 H^2}{48} [\eta^3 + (1-\eta)^3] = \frac{\rho_0 L^2}{12} \left(\frac{fF}{\eta}\right)^2 [\eta + (1-\eta)^3/\eta^2]. \tag{19}$$

For the range $1 \geq \eta \geq 0.5$ used here, the first expression in square brackets varies over range between 0.25 and 1. This estimate (19) of the frontal APE is used as a basis of comparison for the peak eddy kinetic energy in the model runs.

b. Eddy kinetic energy

For each finite-amplitude model run, the peak eddy kinetic energy is extracted and displayed as a function of the slope Burger number *s* (Fig. 13). When these values are
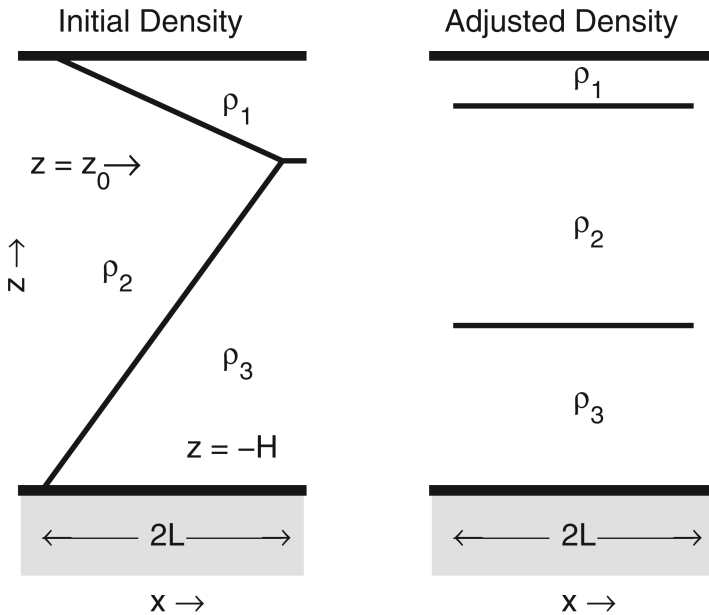
Figure 12. Schematic of the layered frontal geometry used to estimate available potential energy.

normalized using the APE, i.e., by E_0/ρ_0, the scatter in this diagram is considerably reduced, especially for $s = 0$. Consistent with the linear growth rate estimates (14a), the normalized EKE is largest for $s < 0$ and falls off monotonically for $s > 0$. However, the agreement is only qualitative. While linear growth rate falls off as $(1 + 1.5\ s)^{-1}$, the normalized peak EKE is fairly flat for $s < 0$ and falls off much more quickly for $s \geq 0$: as $(1 + 12s)^{-1}$. Nonetheless, it is clear that the efficiency with which APE is converted to EKE is strongly dependent on the bottom slope. Indeed, if one measures energy extraction in terms of the change of height of the model's center of gravity, the cases with $s < 0$ clearly lower the center of gravity more effectively than do the other runs. It is thus interesting to inspect Figure 10 from this perspective: the run with $s > 0$ (Fig. 10b) shows much less redistribution of the density field than does the flat bottom case (Fig. 10a) or runs with $s < 0$ (Fig. 10c).

c. Lateral mixing coefficients

Because of the evolving nature of these initial value problem runs, there is some arbitrariness in estimating a single number to characterize a horizontal mixing coefficient. For the sake of definiteness, lateral mixing is estimated at the time when the horizontal eddy heat flux is at a maximum. This time is chosen because this lateral flux is associated with the transfer from APE to EKE and is clearly identifiable in all model runs. At this time, the midchannel eddy heat and tracer fluxes are estimated near the surface and at mid-depth, as are the mean horizontal gradients. These numbers are then used to compute a horizontal
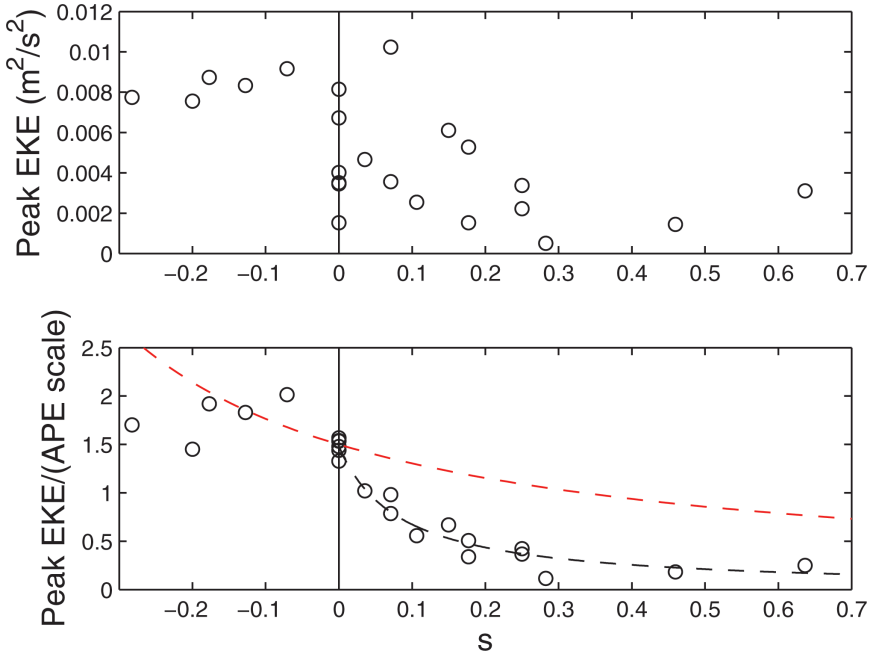
Figure 13. Peak eddy kinetic energy for all finite-amplitude runs as a function of slope Burger number s. Upper panel: unscaled energy. Lower panel: eddy kinetic energy normalized by the available potential energy scale (19). The black dashed curve in the lower panel is $1.5 (1 + 12s)^{-1}$ and the red dashed curve is $1.5 (1 + 1.5s)^{-1}$.

mixing coefficient, e.g., $K = -\{u'T'\}/\{T_x\}$. There is some scatter among the four estimates (temperature and tracer, at two depths each) obtained this way, but the estimates of lateral mixing for a given run are usually consistent to within about 30%. A mean value at the time of maximum heat flux for each run is then recorded. The range of modeled diffusivities, 30–300 m^2 sec^{-1}, is not inconsistent with eddy diffusivities over Georges Bank (150–380 m^2 sec^{-1}), as estimated by Loder *et al.* (1982) using climatological temperature observations.

The resulting eddy coefficient is plotted for each run as a function of s (Fig. 14, upper panel). The glaring asymmetry in the comparable plot for peak EKE (Fig. 13, upper panel) is not apparent. One potential scaling for eddy viscosity might be the product of a typical cross-channel velocity times a typical mixing length scale:

$$K_0 = U L^x \approx (E_0/\rho_0)^{1/2} \eta \Lambda, \tag{20}$$

i.e., the velocity might scale as the square root of available potential energy (as a scale for eddy kinetic energy) times an internal Rossby radius, $\eta \Lambda$. This scaling does reduce the scatter for $s = 0$ (Fig. 14), although not well for $s \neq 0$ (the rms error in an overall fit is 124 m^2 sec^{-1}). However, the scaled values now accentuate the relative symmetry of K/K_0
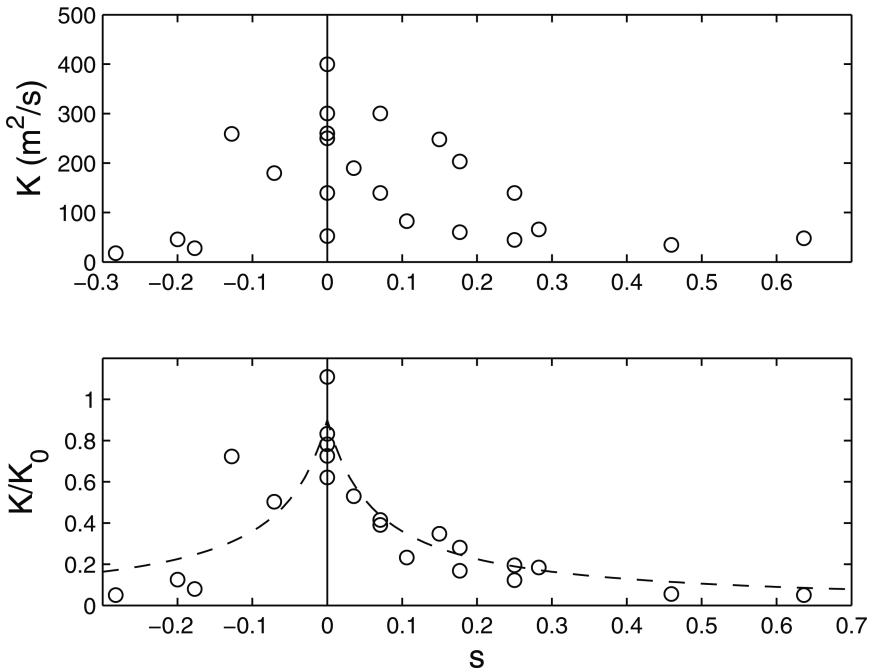
Figure 14. Horizontal eddy exchange coefficient K as a function of slope Burger number s for all finite-amplitude model runs. Upper panel: unscaled eddy coefficients. Lower panel: eddy coefficients scaled by (20). The dashed line in the lower panel is given by $0.9(1 + 15|s|)^{-1}$.

about $s = 0$. Taking the velocity scale to be defined by the thermal wind at the front (13) leads to about as effective a collapse of the points as that from (20). Defining U with the square root of the actual computed peak kinetic energy (top panel of Fig. 13) performs a good deal more poorly. A scaling that accounts for the effects of the bottom slope,

$$K \approx K_0(1 + 15|s|)^{-1}, \tag{21}$$

provides a reasonable (rms error = 50 m^2 sec^{-1}, correlation of 0.85) fit to the calculations and is symmetric about the s axis. Not surprisingly, taking K_0 to be a constant in (21) yields a substantially poorer fit. A physical interpretation of (21) is that the eddy length scale decreases as $|s|$ increases, but the correlation between the length scale $K\ EKE_m^{-1/2}$ (where EKE_m is the maximum eddy kinetic energy per unit mass) and the wavelength of the initial instability is very weak (0.15). The s, hence bottom slope, dependence in (21) is a good deal stronger than in the expression for the most linearly unstable wavelength (14b), just as was found in comparing linear growth rate to peak EKE.

There remains a considerable puzzle here. One might expect that the actual EKE would provide a good velocity scale to use in (20), and certainly better than an estimate based on

the APE. This is not the case. Put another way, on the basis of Figure 13 one would expect a larger eddy mixing coefficient for $s < 0$ than for $s > 0$. This would have been intuitive, as well, based on the larger linear growth rates for $s < 0$. Clearly, the mixing is less efficient relative to EKE for $s < 0$ than for $s > 0$. A number of possibilities were explored to explain this decreased mixing efficiency, including a lesser velocity-scalar correlation, and velocity anisotropy (making EKE a poor estimate of cross-channel velocity). However, a satisfactory explanation was not found. It is important to note that Isachsen (2011) treated the sustained instability of a buoyancy current front over shelf-slope topography and found a similar crude symmetry of the lateral mixing coefficient with regard to his measure of the bottom slope. Because Isachsen (2011) maintained his model buoyancy current with surface heat fluxes, the lateral mixing was sustained for a long period, and so his estimates of K were statistically very robust.

One potential explanation for the peculiar behavior of the lateral mixing coefficients is to be found in Green (1970) or Klocker *et al.* (2012), for example. Specifically, they find that if eddies propagate along-channel relative to the mean flow, this can suppress the net mixing across a jet. Physically, the eddy pattern is not entirely random, but rather, the orderly translating structure of the propagating eddies makes turbulent cross-stream transport less efficient. On the basis of Klocker *et al.*, one might expect that the scaling for a basic estimate of eddy diffusivity (20) would be improved by modifying it to be

$$K_C \approx (E_0/\rho_0)^{1/2} \eta \Lambda [1 + \theta (U - c)^2]^{-1}, \tag{22}$$

where θ is a constant to be determined. The jet velocity U is taken to be the most negative along-channel/time-averaged velocity over the two days centered on the time when K is estimated. The eddy propagation velocity c is estimated at the same time using y-lagged correlations of midchannel u records lagged by one day. In all cases, $c < 0$. The conjectured suppression at the jet axis (channel center) is tested by comparing computed K with those derived from (20) alone to those from (22), i.e., not using the empirical correction for bottom slope (21). The result is that (20) gives a least squares fit with error 124 m^2 sec^{-1} (correlation 0.04), while the error of (22) is 97 m^2 sec^{-1} (correlation 0.44). Thus, because (22) is an improvement over (20), it seems likely that at least part of the peculiarity in the eddy coefficient vs. *EKE* scaling is associated with this effect. However, this effect seems not to represent a complete explanation of the phenomenon, because the empirically based fit (21) clearly performs better.

6. Conclusions

The present study concentrates on the stability of an idealized steady tidal mixing front under the assumptions of no bottom friction and initial vorticities that are stable with regard to symmetric instabilities. Obviously, a realistic tidal mixing frontal model would have to deal with frictional dissipation, a front that is potentially rather sharp, and tidal time dependence. Future communications will deal with these added effects. The objective of

the present study is to understand the basic stability properties of this frontal configuration, and so to understand how factors such as bottom slope, latitude and stratification affect the strength and evolution of the instability.

The linear stability model is used to assess the dependence of initial instability (growth rate and wavelength) on the model configuration. All of the cases examined are unstable. The initial instabilities in this problem are clearly baroclinic, in that initial potential energy associated with the stratification is transferred into eddy potential and kinetic energy. The results collapse cleanly to expressions (14) that encapsulate how, for example, the basic Rossby radius length scale is modified by including a sloping bottom. The results of the linear stability calculations agree well with initial growth rates in more realistic finite-amplitude evolution models.

The finite-amplitude models are executed using a primitive equation numerical model, and the temporal evolution consistently involves a transitory peak in eddy kinetic energy. The fields eventually evolve, via an inverse cascade, toward an apparently baroclinically stable state where the frontal jet has been replaced by an energetic mean flow that is laterally sheared on the scale of the channel width. Consistent with the linear growth rates, the peak eddy kinetic energy is greatest when the initial near-bottom isopycnals slope in the same sense as the bottom. Unlike the maximum eddy kinetic energy (which is strongly dependent on the direction of the bottom slope), the eddy mixing coefficients decrease with increasing bottom slope magnitude, regardless of the slope's sign. Because one might expect that the mixing coefficients would scale with the square root of the actual eddy kinetic energy, it is not at all apparent why the mixing coefficients and eddy kinetic energy should behave so strikingly differently.

One of the main questions driving the present study is whether cross-frontal nutrient transports due to eddy exchange are comparable to those suggested by the two-dimensional model of Franks and Chen (1996). Their net nutrient transport due to two-dimensional processes apparently amounts to about 1,200 mol Nut day^{-1} (their nutrient "Nut" is identified with Nitrogen). One can estimate the cross-front flux due to eddy mixing using a cross-frontal gradient of dissolved nutrient (Franks and Chen, 1996) of 0.6 μM Nut m^{-4}, and an eddy coefficient of 30–300 m^2 sec^{-1} (Fig. 14). These values lead to an estimated flux of 400–4,000 mol Nut day^{-1}, which brackets the Franks and Chen estimate. One should not take this lateral flux estimate too seriously. For one thing, this is representative of only the moment of peak cross-frontal flux in the present initial value problem. It is far more relevant to work with estimates from a model in statistical steady state. Further, the present model is highly idealized, in that it does not include bottom friction, a time-dependent front nor atmospheric fluxes. Nonetheless, this crude estimate of cross-frontal flux is not inconsistent with the possibility of an eddy flux mechanism being a substantial contributor to nutrient supply to a tidally mixed region. These idealizations will be addressed in future contributions.

In summary, all of the idealized frontal configurations considered here are found to be unstable. The quantities that determine the instability's properties include frontal width,

ambient stratification, water depth and the bottom slope (measured here by a slope Burger number). The finite amplitude of the evolution follows a path that might be expected on the basis of quasigeostrophic results (e.g., Rhines, 1977): both vertical and horizontal scales increase until a limit (channel width or Rhines scale) is reached. Thus the main findings of this contribution are that 1) this frontal configuration, although not inherently describable in terms of quasigeostrophy, evolves in the expected way, and that 2) the instability is sufficiently energetic (in terms of growth rate of eddy diffusivity) that it has potential to help account for observed lateral fluxes in tidally dominated regions.

REFERENCES

Badin, G., R.G. Williams, J.T. Holt and L.J. Fernand, 2009: Are mesoscale eddies in shelf seas formed by baroclinic instability of tidal fronts? *J. Geophys. Res*., 114, C10021, doi:10.1029/2009JC005340.

Barth, J.A., 1989. Stability of a coastal upwelling front, 2, Model results and a comparison with observations. J. Geophys. Res., *94*, 10857–10883.

Blumsack, S.L. and P.J. Gierasch, 1972: Mars: the effects of topography on baroclinic instability. J. Atmos. Sci., *29*, 1081–1089.

Brink, K. H., 2006. Coastal-trapped waves with finite bottom friction. Dynamics of Atmospheres and Oceans, *41*(3–4), 172–190.

Chen, C., R.J. Schlitz, R.G. Lough, K.W. Smith, R. Beardsley, and J.P. Manning, 2003: wind-induced, cross-frontal exchange on Georges Bank: a mechanism for early summer on-bank biological particle transport. J. Geophys. Res., *108*(C11), doi:10.1029/2002JC001358.

Flierl, G.R., and J. Pedlosky, 2007: The nonlinear dynamics of time-dependent subcritical baroclinic currents. J. Phys. Oceanogr., *37*, 1001–1021.

Franks, P.J.S. and C. Chen, 1996. Plankton production in tidal fronts: a model of Georges Bank in summer, J. Marine Res., *54*, 631–651.

Garrett, C.J.R., and J. Loder, 1981: Dynamical aspects of shallow sea fronts. Phil. Trans. R. Soc. Lond. A, *302*, 563–581.

Green, J.S.A., 1970. Transfer properties of the large-scale eddies and the general circulation of the atmosphere. Quart J. R. Met. Soc., *96*, 157–185.

Isachsen, P.E., 2011: Baroclinic instability and eddy tracer transport across sloping bottom topography: how well does a modified Eady model do in primitive equation simulations?. Ocean Modelling, *39*, 183–199.

James I.D., 1989b: A three-dimensional model of circulation in a frontal region of the North Sea. Dtsch. Hydrogr. Z. *42*, 231–247.

Klocker, A., R. Ferrari and J.H. LcCasce, 2012. Estimating suppression of eddy mixing by mean flows. J. Phys. Oceanogr., *42*, 1566–1576.

Loder, J.W., D. Brickman and E.P.W. Horne, 1992: Detailed structure of currents and hydrography on the northern side of Georges Bank. J. Geophys. Res., *97*(C9), 14,331–14,351, doi:10.1029/92JC01342.

Loder, J.W., and D.G. Wright, 1985: Tidal rectification and frontal circulation on the sides of Georges Bank. J. Marine Res., *43*, 581–604.

Loder, J.W., D.G. Wright, C. Garrett and B.-A. Juszkoi, 1982. Horizontal exchange on central Georges Bank. Can. J. Fish. Aquat. Sci. *39*: 1130–1137.

Pedlosky, J., 1979: Geophysical Fluid Dynamics. Springer-Verlag, New York, 624pp.

Poulin, F.J., G.R. Flierl and J/ Pedlosky, 2003: Parametric instability in oscillatory shear flows. J. Fluid Mech., *481*, 329–353.

Rhines, P.B., 1975: Waves and turbulence on a β-plane. J. Fluid Mech., *69*, 417–443.

Rhines, P.B., 1977: The dynamics of unsteady currents. In *The Sea*, volume 6, 189–318.

Roullet, G., J.C. McWilliams, X. Capet, and M.J. Molemaker, 2012: Properties of steady geostrophic turbulence with isopycnal outcropping. J. Phys. Oceanogr. *42*, 18–38.

Shchepetkin, A.F., and J.C. McWilliams, 2005: The regional oceanic modeling system (ROMS): A split-explicit, free-surface, topography-following-coordinate oceanic model. Ocean Modelling, *9* (4), 347–404.

Simpson, J.H. and J.R. Hunter, 1974: Fronts in the Irish Sea. Nature, *250*, 404–406.

Simpson, J.H., and I.D. James, 1986: Coastal and estuarine fronts. In *Baroclinic Processes on Continental Shelves* (C.N.K. Mooers, editor), American Geophysical Union, Washington D.C., 63–94.

Stone, P.H., 1966: On non-geostrophic baroclinic instability. J. Atmos. Sci., *23*, 390–400.

Thomas, P.J. and P.F. Linden, 1996: A laboratory model simulation of mixing across tidal fronts. J. Fluid Mech., *309*, 321–344.

van Heijst, G.J.F., 1986: On the dynamics of a tidal mixing front. In *Marine Interfaces Ecohydrodynamics*, (J.C.J. Nihoul, editor), Elsevier Oceanography Series, *42*, 165–194.

Wijesekera, H. W., J. S. Allen, and P. Newberger, 2003: A modeling study of turbulent mixing over the continental shelf: Comparison of turbulent closure schemes. J. Geophys. Res., *108* (*C*3), 3103, doi:10.1029/2001JC001234.